Comparison of a numerical model with measured performance of a seeded, nanosecond KTP optical parametric oscillator

A. V. Smith, W. J. Alford, and T. D. Raymond

Laser, Optics, and Remote Sensing Department, Sandia National Laboratories, Albuquerque, New Mexico 87185-0601

Mark S. Bowers

Aculight Corporation, 40 Lake Bellevue, Suite 100, Bellevue, Washington 98005

Received February 7, 1995; revised manuscript received April 26, 1995

We have constructed a numerical model of seeded optical parametric oscillators that is appropriate for nanosecond or longer pulsed operation. We have also experimentally characterized the performance of a KTP ring optical parametric oscillator. We present a description of the model and show that its predictions agree well with the observed oscillator performance. We compare spatial beam quality, spectra, efficiency, and full-beam and spatially resolved temporal profiles. Backconversion of signal and idler light to pump is found to affect all the aspects of performance. © 1995 Optical Society of America

1. INTRODUCTION

Nanosecond pulsed optical parametric oscillators (OPO's) hold great promise as sources of coherent yet widely tunable light. They were first demonstrated 30 years ago,[1] but for many years their development was stymied by the lack of suitable nonlinear crystals, cavity optics, and pump lasers. The recent resurgence of activity in the field[2–20] has been stimulated by the development of new crystals such as potassium titanyl phosphate (KTP), lithium triborate (LBO), and β-barium borate, by the development of single-longitudinal-mode pump lasers, and by progress in high-damage-threshold optics. Despite recent progress, these devices have yet to reach their potential as sources with narrow linewidth, broad tunability, and good beam quality. One of the reasons is that their behavior is more complex than is often appreciated. In contrast to lasers, OPO's are sensitive to the phase of the pump light because it can be impressed on the signal and the idler waves. Additionally, they have no gain storage time, so the single-pass gain must be high if the pump-pulse duration is limited to a few nanoseconds. Such high gain often results in strong conversion of signal and idler waves back into the pump waves. This backconversion can strongly influence the efficiency, the beam quality, and the spectra of OPO-generated light. Another distinction between lasers and OPO's is the use of critically phase-matched crystals in OPO's. These crystals introduce angular sensitivity of the gain, with the consequence that there is an acceptance angle or a maximum allowed angular spread of the three interacting waves imposed by the crystal in addition to that imposed by other cavity optics. Furthermore, parametric oscillator performance is sensitive to cavity feedback of signal, idler, and pump waves and can be strongly influenced by small amounts of unwanted feedback.

Because of the daunting array of variables that must be considered in designing on OPO, we have developed a numerical model of OPO performance as a design tool that allows us to alter any of the variables quickly and to study the resulting changes in beam quality, efficiency, time profiles, and spectra. To benchmark the model we have made a careful laboratory study of the performance of a particular OPO and have compared it with the model's predictions. The model includes all the relevant physics for a seeded, nanosecond OPO pumped by a single-frequency pump laser. We account for the nonlinear interaction in the crystal, including pump depletion, birefringence, diffraction, realistic spatial and temporal beam profiles, signal- or idler-wave seeding of the oscillator cavity, arbitrary cavity-mirror reflectivities, and absorptive losses in the crystal. The laboratory measurements encompassed efficiencies, energy fluence transverse profiles, spatially resolved and spatially integrated power profiles, and output spectra for careful characterization of operating conditions. We report here on the comparison between the model predictions and the laboratory measurements and show that our model is successful in describing actual OPO performance.

2. NUMERICAL MODEL

Despite the long history of OPO's and the recent flurry of research activity, there have been few published reports of modeling that is applicable to nanosecond OPO's. Because these devices operate in the transient regime, models developed for cw OPO's cannot accurately predict their behavior. In one model that is appropriate to pulsed OPO's, Brosnan and Byer[21] used analytic expressions for parametric gain to describe nondiffracting waves in the limit of low pump depletion. This model

0740-3224/95/112253-15$06.00

was used to predict threshold pump fluences. Later variations on this model by Guha *et al.*[22] and by Terry *et al.*[23] add optical cavity modes and crystal birefringence to the analysis but retain the assumption of low pump depletion. Because of this approximation, these models predict only threshold energies or fluences. Once the pump exceeds threshold by a small amount, the assumption of low pump depletion is violated, so these models cannot predict other properties of OPO's, such as conversion efficiencies, power profiles, or beam quality. In a recent paper, Breteau *et al.*[24] numerically modeled a KTP, linear-cavity OPO pumped by 12-ns pulses from a *Q*-switched Nd:YAG laser. Their model is based on numerical integration of the frequency-mixing equations for plane waves. It neglects spatial beam profiles, walk-off, and diffraction. Nevertheless, by adjusting the value of the nonlinear coefficient d_{eff}, they achieve good agreement with the measured power profiles and efficiencies for a multilongitudinal-mode OPO described in the same report. Our model takes the next step and includes transverse profiles, diffraction, and walk-off.

A conceptual description of our model is now given. All radiation within the cavity is approximated by a series of time slices separated by the round-trip time for the OPO cavity. Evolution of these slices is calculated by solution of the paraxial Maxwell equations in retarded time as the slices propagate around the OPO cavity. For each time slice, the transverse profile of the pump optical field is constructed on a rectangular mesh and is propagated to the OPO's input mirror, where it is combined with the pump light already in the cavity. The resulting pump field is again propagated around the optical cavity back to the input mirror, and this process is repeated for the duration of the pump pulse. The same procedure is applied to the seeded signal wave. The third wave, the idler, is generated entirely within the OPO cavity. All propagation includes diffraction handled by fast-Fourier-transform methods, allowing us to track the phases and the amplitudes of all three waves over their transverse profiles. The modeling of the nonlinear interaction of the three waves in the mixing crystal accounts for diffraction, linear absorption, phase velocity mismatch, and strong energy exchange among the three waves. We assume that the crystal is uniaxial. This assumption is also sufficient for biaxial crystals if they are oriented for propagation in one of the principal planes, as is usually the case. The result is a record of the phase and the amplitude of each optical field at the OPO input and output mirrors on a transverse spatial grid and a time grid (which is set by the round-trip time). From this time log of the fields we derive the powers as a function of time, the transverse intensity profiles at any propagation distance, beam quality (as measured by Siegman's[25,26] M^2), and wave-front tilt and curvature. We can also find the time development of the intensities at any point in the transverse profile, plus fluence profiles and spectra. We find the spectra by Fourier transforming the fields separately for each spatial location and summing them.

This time-slice approach assumes that all three waves have the same group velocity and is thus usually not appropriate for picosecond or shorter pulses. It also assumes that there are no frequency-selective elements such as étalons or gratings in the cavity. Strictly speaking, this approach is appropriate only for nanosecond or longer, seeded OPO's. Even for this case, under some conditions, the model predicts sharp, picosecond-scale time variations. Clearly, caution must be exercised in interpreting such results. Fortunately, these sharp features are absent unless the OPO is driven far above threshold, at levels that are not of practical interest. Although the model has a bandwidth or pulse-width limit imposed because it ignores group-velocity dispersion, it may still be useful, if not exact, for OPO's that weakly violate our assumptions.

The key to implementing the model is integration of the signal, the idler, and the pump waves through the mixing crystal, allowing for birefringence, pump depletion, and diffraction. This problem cannot be solved analytically, so we use numerical methods similar to those described in the literature.[27–30] Our methods are documented in a previous paper.[31] Briefly, in a birefringent crystal, the Poynting vector for waves with extraordinary polarization is tilted by the walk-off angle ρ relative to its k vector. In our laboratory coordinate system, the optic axis of the uniaxial crystal lies in the x–z plane. The k vectors nominally point in the z direction, so x-polarized, or extraordinary, light walks off in the x direction, but y-polarized, or ordinary, light does not walk off. In the paraxial approximation, if we ignore the slight asymmetry of diffraction in the x and the y directions, the mixing equations take the form

$$\frac{\partial \varepsilon_j(x, y, z, t)}{\partial z} = \frac{i}{2k_j}\left[\frac{\partial^2 \varepsilon_j(x, y, z, t)}{\partial y^2} + \frac{\partial^2 \varepsilon_j(x, y, z, t)}{\partial x^2}\right] - \tan(\rho_j)\frac{\partial \varepsilon_j(x, y, z, t)}{\partial x} + \mathcal{P}_j(x, y, z, t) - \alpha_j \varepsilon_j(x, y, z, t), \tag{1}$$

where j indexes the frequency (signal, idler, or pump). The complex variable ε is a Fourier component of the optical electric field E_j, defined by

$$E_j = {}^1\!/\!_2\{\varepsilon_j \exp[-i(\omega_j t - k_j z)] + {\varepsilon_j}^* \exp[i(\omega_j t - k_j z)]\}. \tag{2}$$

The linear loss in the crystal is α, and the nonlinear polarization drive term $\mathcal{P}_j(x, y, z, t)$ is defined by

$$\mathcal{P}_s(x, y, z, t) = i\frac{d_{\text{eff}}\omega_s}{cn_s}\varepsilon_p(x, y, z, t){\varepsilon_i}^*(x, y, z, t) \times \exp(i\Delta k z), \tag{3a}$$

$$\mathcal{P}_i(x, y, z, t) = i\frac{d_{\text{eff}}\omega_i}{cn_i}\varepsilon_p(x, y, z, t){\varepsilon_s}^*(x, y, z, t) \times \exp(i\Delta k z), \tag{3b}$$

$$\mathcal{P}_p(x, y, z, t) = i\frac{d_{\text{eff}}\omega_p}{cn_p}\varepsilon_i(x, y, z, t)\varepsilon_s(x, y, z, t) \times \exp(-i\Delta k z), \tag{3c}$$

where

$$\Delta k = k_p - k_s - k_i. \tag{4}$$

These equations are integrated through the crystal by transformation to retarded-time coordinates, where $z =$

ct/n. Thus z and t are not independent variables. Instead, t can be considered an index on the time slices. Fourier transforming the electric fields and the polarization terms in the transverse dimension, using

$$\varepsilon_j(x, y, z, t) = \int_{-\infty}^{\infty} \tilde{\varepsilon}_j(s_x, s_y, z, t) \times \exp[i2\pi(s_x x + s_y y)]\mathrm{d}s_x \mathrm{d}s_y\,, \qquad (5)$$

$$\mathcal{P}_j(x, y, z, t) = \int_{-\infty}^{\infty} \tilde{\mathcal{P}}_j(s_x, s_y, z, t) \times \exp[i2\pi(s_x x + s_y y)]\mathrm{d}s_x \mathrm{d}s_y\,, \qquad (6)$$

and substituting these definitions of $\varepsilon_j(x, y, z, t)$ and $\mathcal{P}_j(x, y, z, t)$ into Eq. (1), we arrive at the following equation for the propagation of the individual spatial-frequency component waves:

$$\frac{\partial \tilde{\varepsilon}_j(s_x, s_y, z, t)}{\partial z} = -i\left[\frac{2\pi^2}{k_j}({s_x}^2 + {s_y}^2) + 2\pi s_y \tan(\rho_j)\right] \times \tilde{\varepsilon}_j(s_x, s_y, z, t) + \tilde{\mathcal{P}}_j(s_x, s_y, z, t)\,. \qquad (7)$$

We now have three coupled first-order differential equations describing the change in each spatial-frequency component of the fields as they propagate through the crystal. The coupling is by means of the nonlinear interaction term $\tilde{\mathcal{P}}_j(s_x, s_y, z, t)$.

We integrate Eq. (7), using the Cash–Karp Runge–Kutta algorithm.[32] At the beginning of each z step, the $\tilde{\varepsilon}_j(s_x, s_y, z, t)$ terms are Fourier transformed to give $\varepsilon_j(x, y, z, t)$. These terms are used in Eqs. (3) to calculate the polarization drive terms $\mathcal{P}_j(x, y, z, t)$, which are Fourier transformed to yield the $\tilde{\mathcal{P}}_j(s_x, s_y, z, t)$'s of Eq. (7). The x–y spatial grid is typically 32×32 or 64×64, and the integration of a single time slice through the crystal is performed in approximately 32 steps. The number of time slices is typically 75. Run time on a Pentium-based computer is of the order of 1000 s.

In a previous paper[31] we showed formulas for computing the beam-quality factor M^2, the spot size, and other beam parameters as functions of time from this type of modeling. Although useful in illuminating the dynamics of the OPO, these quantities are difficult to measure for nanosecond pulses. However, their time-integrated counterparts are measurable and are usually the quantities of interest. Thus it would be useful to define similar time-integrated quantities to characterize the fluences, or the time-integrated intensities. Here we present formulas for calculating these quantities. The derivation is similar to our previous one, except the transverse moments of the optical pulse in both the spatial and the spatial-frequency domains are now based on the intensity integrated over time (the energy fluence distribution). We start by defining the quantity U as

$$U = \int_{-\infty}^{\infty}\int_{-\infty}^{\infty}\int_{-\infty}^{\infty} |\varepsilon(x, y, t)|^2 \mathrm{d}x\mathrm{d}y\mathrm{d}t = \int_{-\infty}^{\infty}\int_{-\infty}^{\infty}\int_{-\infty}^{\infty} |\tilde{\varepsilon}(s_x, s_y, t)|^2 \mathrm{d}s_x \mathrm{d}s_y \mathrm{d}t\,, \qquad (8)$$

where s_x is $k_x/2\pi$ or the x transverse component of the spatial-frequency vector. The first moments in the spatial and the spatial-frequency domains are now defined in terms of fluence rather than intensity:

$$\overline{x}(z) = \frac{1}{U}\int_{-\infty}^{\infty}\int_{-\infty}^{\infty} x\left[\int_{-\infty}^{\infty} |\varepsilon(x, y, z, t)|^2 \mathrm{d}t\right]\mathrm{d}x\mathrm{d}y\,, \qquad (9)$$

$$\overline{s}_x = \frac{1}{U}\int_{-\infty}^{\infty}\int_{-\infty}^{\infty} s_x\left[\int_{-\infty}^{\infty} |\tilde{\varepsilon}(s_x, s_y, t)|^2 \mathrm{d}t\right]\mathrm{d}s_x\mathrm{d}s_y\,. \qquad (10)$$

One can show that the first spatial moment propagates according to

$$\overline{x}(z) = \overline{x}(0) + \lambda z \overline{s}_x\,. \qquad (11)$$

Similarly, the fluence-based variances are given by

$$\sigma_x{}^2(z) = \frac{1}{U}\int_{-\infty}^{\infty}\int_{-\infty}^{\infty} [x - \overline{x}(z)]^2\left[\int_{-\infty}^{\infty} |\varepsilon(x, y, z, t)|^2 \mathrm{d}t\right] \times \mathrm{d}x\mathrm{d}y\,, \qquad (12)$$

$$\sigma_{s_x}{}^2 = \frac{1}{U}\int_{-\infty}^{\infty}\int_{-\infty}^{\infty} (s_x - \overline{s}_x)^2\left[\int_{-\infty}^{\infty} |\tilde{\varepsilon}(s_x, s_y, t)|^2 \mathrm{d}t\right] \times \mathrm{d}s_x\mathrm{d}s_y\,. \qquad (13)$$

The x variance can be shown to propagate according to

$$\sigma_x{}^2(z) = \sigma_x{}^2(0) - [A_x(0) + 2\lambda\overline{x}(0)\overline{s}_x]z + \lambda^2 \sigma_{s_x}{}^2 z^2\,, \qquad (14)$$

where

$$A_x(z) = \frac{\lambda}{\pi U}\int_{-\infty}^{\infty}\int_{-\infty}^{\infty} x \times \left\{\int_{-\infty}^{\infty} \mathrm{d}t\ \mathrm{Im}\left[\varepsilon(x, y, z, t)\frac{\partial \varepsilon^*(x, y, z, t)}{\partial x}\right]\right\} \times \mathrm{d}x\mathrm{d}y\,. \qquad (15)$$

The formulas for the fluence-based minimum variance or beam waist, $\sigma_{0x}{}^2$; for the beam-quality factor, M^2; and for the radius of curvature in the x dimension become

$$\sigma_{0x}{}^2 = \sigma_x{}^2(z) - \frac{[A_x(z) + 2\lambda\overline{x}(z)\overline{s}_x]^2}{4\lambda^2\sigma_{s_x}{}^2}\,, \qquad (16)$$

$$M_x{}^2 = 4\pi\sigma_{0x}\sigma_{s_x}\,, \qquad (17)$$

$$R_x(z) = \frac{-2\sigma_x{}^2(z)}{A_x(z) + 2\lambda\overline{x}(z)\overline{s}_x}\,, \qquad (18)$$

respectively. Similar equations describe the beam properties in the transverse y dimension.

We can summarize the numerical calculations of the OPO as follows. We numerically integrate the wave equations, Eq. (7), for pancakes of light propagating through the crystal and around the cavity. The wave equations include all the relevant physics of the problem, including crystal birefringence, diffraction, and pump depletion. The result of this calculation is a record of the electric-field amplitude and the phase for each of the three waves emerging from the OPO cavity, from which properties such as spectra, time profiles, spatial profiles, and beam quality are calculated.

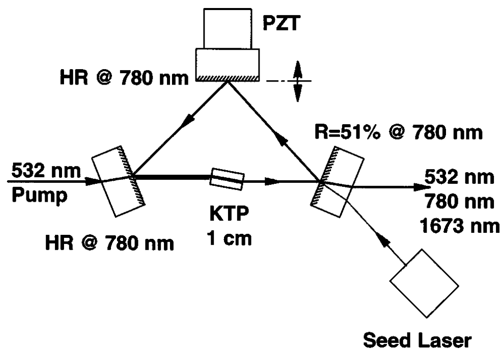

Fig. 1. Schematic diagram of laboratory KTP ring OPO. HR, high reflector.

3. LABORATORY MEASUREMENTS

In this section we describe our laboratory OPO and explain how the measurements were made. We chose as an OPO cavity the simple three-mirror ring configuration shown in Fig. 1, rather than a two-mirror linear configuration, primarily to reduce unwanted feedback of the pump and the idler waves and thereby ensure that the cavity is truly singly resonant. This geometry also reduces unwanted optical feedback to the seed laser and tends to average signal beam inhomogeneities in the plane of the ring because the image reverses on every round trip. The three cavity mirrors are flat and are arranged so that the total cavity length is 6.7 cm. The signal, the idler, and the pump wavelengths are 780, 1673, and 532 nm, respectively. At 780 nm, two of the mirrors are high reflectors, whereas the third has 51% reflectivity. One of the high reflectors is mounted on a piezoelectric transducer to permit fine adjustment of the cavity length to resonate the 780-nm seed light. The round-trip loss at the pump and the idler wavelengths is greater than 99.9%. The nonlinear medium is a 1-cm-long KTP crystal cut at $\theta = 51°$, $\phi = 0°$ for Type-II phase matching. It is mounted on a rotation stage so that it can be rotated about an axis perpendicular to the plane of the ring. The crystal is antireflection coated for 780 and 532 nm. The resonated signal wave at 780 nm is polarized in the plane of the ring cavity and propagates through the crystal as an extraordinary wave. The pump and the idler waves are polarized perpendicular to the plane of the ring and are ordinary waves. Thus the critical direction for phase matching coincides with the plane of the ring. The signal-wave walk-off is 0.51 mm in the plane of the resonator.

Figure 2 is a schematic of the entire experiment. The OPO is pumped by spatially filtered 532-nm pulses. The 1064-nm light from the oscillator of a Q-switched, injection-seeded Nd:YAG laser (Continuum NY61) is frequency doubled in either a 2-cm-long LBO crystal or an 8-mm-long KTP crystal, and the second-harmonic light is focused with a 1-m focal-length lens onto a 400-μm-diameter diamond pinhole for spatial filtering. A telescope collimates the light to a 0.6-mm (FWHM) beam with a pulse energy of as much as 12 mJ. This value corresponds to pump fluences of as much as 2.5 J/cm^2 (300 MW/cm^2). The duration of the 532-nm pulse is set to 6–8 ns FWHM and is controlled by variation of the Q-switch delay of the Nd:YAG laser. The resulting pump pulse has a slightly shorter rise time than fall time and a fluence profile closely approximated by a Gaussian distribution. Figure 3 shows measured time and fluence profiles fitted by Gaussians.

The OPO is injection seeded with a cw, single-mode Ti:sapphire laser (Schwartz Electro-Optics model Titan CWBB) pumped by an argon-ion laser (Spectra-Physics Model 2020). The Ti:sapphire laser produces light with a near-TEM$_{00}$ mode that is magnified, collimated, and passed through an iris to produce a seed beam with an Airy central disk with a FWHM of 1 mm at the OPO and a power of typically 10–40 mW. This value is much larger than the approximately 10-nW minimum that we find is required for seeding the OPO. The measured linewidth of the seed laser is less than 30 MHz. The OPO cavity is adjusted to resonate the seed light by a standard cavity-length dithering technique with a lock-in stabilizer (Lansing 80.215). When measuring the OPO output spectra, we prevented frequency jitter caused by cavity-length dither by firing the Nd:YAG laser when the OPO cavity was exactly resonant with the seed light.

The light generated by the OPO is diagnosed by use of a variety of instruments. CCD cameras connected to a beam-profiling system (Big Sky Analyzer Plus) record fluence profiles of the signal and the depleted pump beams 30 cm away form the output coupler. Fast photodetectors (Hamamatsu R1193 and 1328U, New Focus 1611) record both spatially integrated and spatially resolved power profiles for the incident pump, the depleted pump,

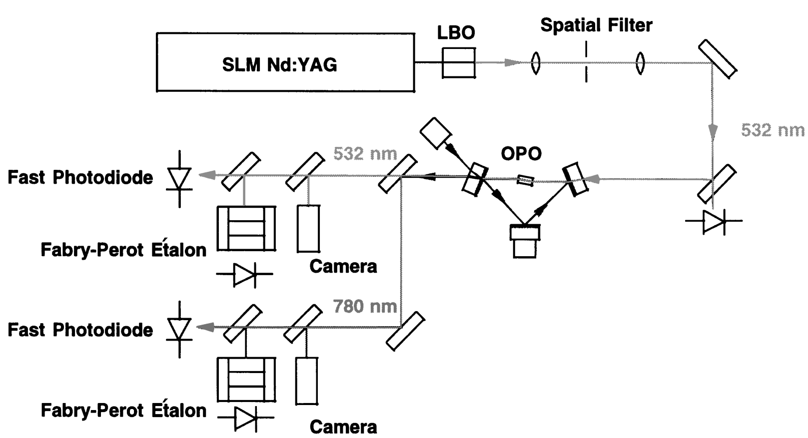

Fig. 2. Schematic diagram of OPO experiment. SLM, single longitudinal mode.

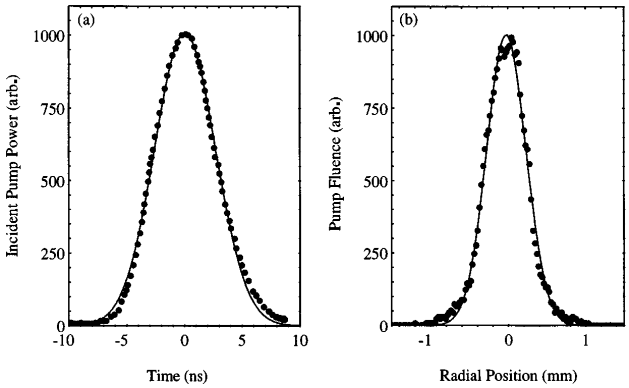

Fig. 3. Power (a) and fluence (b) profiles of the incident pump beam. The dots represent the experimental data, and the curves are least-squares fits of Gaussians to the experiment.

the signal beam, and the idler beam. The OPO signal energy is measured with a pyroelectric detector (Laser Precision Rj-7200), and the incident pump energy is measured with a calorimeter (Scientec 300100). Spectra of the signal and the pump (incident and depleted) waves are obtained by use of high-finesse (>50) scanning Fabry–Perot étalons with free spectral ranges of approximately 1 GHz.

Beam-quality measurements are performed with the beam-profiling system mentioned above to record profiles at various positions through a mild focus formed by a long-focal-length lens. Each profile is analyzed to obtain waist sizes, w_x and w_y, in the two transverse dimensions, x and y. The variation of the waist size with propagation distances, z, is then fitted to the following expression,[26] which describes propagation of a beam with a beam-quality factor of M^2:

$$w^2(z) \equiv 4\sigma^2(z) = w_0{}^2 + \left[\frac{M^2\lambda(z - z_0)}{\pi w_0}\right]^2, \qquad (19)$$

where z_0 is the position of the minimum waist size, w_0, and λ is the wavelength. Note that a beam with a Gaussian spatial distribution and a uniform phase front has $M^2 = 1$, whereas real beams have $M^2 \geq 1$.

4. RESULTS AND DISCUSSION

A. Optical Parametric Oscillator Operating Parameters

Apart from the efficiency, the threshold, and the beam-quality measurements, we compare model and laboratory results at two values of the pump fluence; the lower is 1.6 J/cm^2 or 2.3 times threshold, and the higher is 2.5 J/cm^2 or 3.5 times threshold. The other parameters of importance are described in Appendix A, along with estimates of their experimental uncertainties. These parameters comprise all those used in the model. We used only measured input parameters, making no adjustments to match the actual performance of the OPO. In addition, all the comparisons are on absolute scales unless otherwise indicated.

B. Threshold and Efficiency

The measured and the predicted signal energy and efficiency are plotted in Fig. 4, for both seeded and unseeded operation of the OPO. Each data point represents a single laser pulse. The predicted results for the unseeded OPO are obtained with an incident seed power of 10 nW, the minimum power observed to seed the cavity when the cavity is resonant with the seed frequency. One benefit of seeding that is apparent in these plots is a reduction of the threshold pump energy. This result is expected because the high seed power (30 mW) produces a signal intensity in the OPO cavity that is approximately 6 orders of magnitude above the quantum-noise value of 1 photon/mode. The oscillator thus requires less gain to achieve threshold when it is seeded. Figure 4 also illustrates a reduced shot-to-shot variation of the OPO output energy with seeding.

The seeded (unseeded) signal efficiency, defined as the signal energy out divided by the pump energy in, peaks at approximately 29% (21%), corresponding to a quantum efficiency (signal photons out/pump photons in) of approximately 43% (31%). The model reproduces the seeded operation of the OPO but is less successful in predicting the unseeded performance. This result is

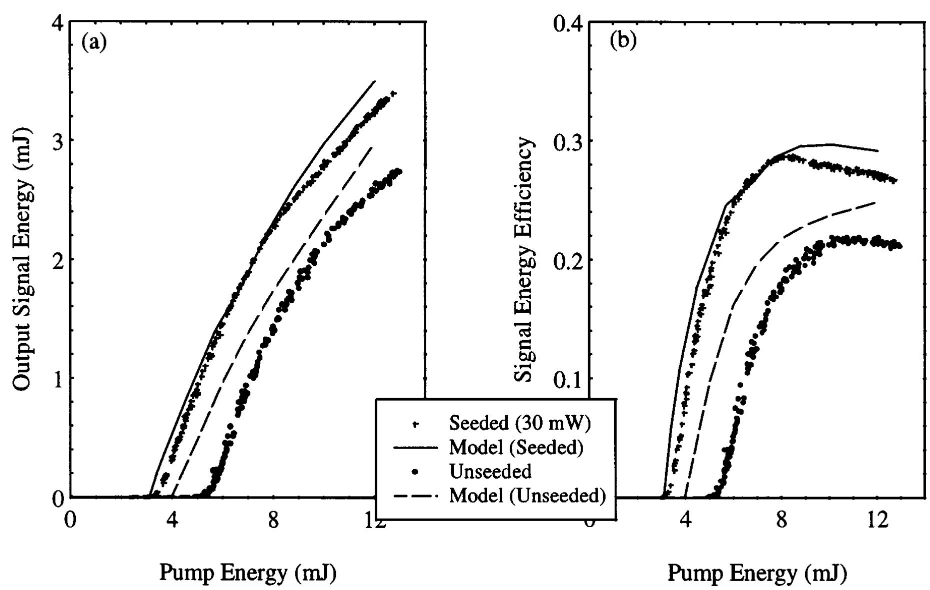

Fig. 4. Measured and predicted output (a) signal energy and (b) efficiency are shown for both seeded and unseeded operation. Note that when the OPO is seeded both the threshold is reduced and the efficiency is increased.

presumably due to the multiple-longitudinal-mode operation of the unseeded OPO and the quantum-noise character of the seed, both of which are not accounted for in the numeric model. The model assumes a classical, monochromatic seed wave, whereas the unseeded device is seeded by quantum noise at both the signal and the idler wavelengths. In addition, at the observed unseeded linewidth of approximately 3 cm^{-1}, our approximation of zero group-velocity dispersion begins to fail. In the remainder of this paper we consider only seeded operation of the OPO.

C. Fluence Profiles

Contour plots comparing measured and calculated energy fluence profiles for the signal and the depleted pump beams are presented in Figs. 5 and 6 for the low (1.6 $\mathrm{J/cm^2}$) and the high (2.5 $\mathrm{J/cm^2}$) pump fluences, respectively. When one recalls that the incident pump beam is nearly Gaussian, it is clear from the depleted pump contours [Figs. 5(a) and 6(a)] that the parametric process has distorted the pump beam asymmetrically with respect to the critical and the noncritical planes. In addition, the distortion is greater at the higher pump level. The signal beam is relatively unstructured at the lower pump fluence but develops side lobes in the noncritical direction at the higher fluence in both the model and the experimental profiles [Figs. 6(c) and 6(d)].

Insight gained from the data and the model leads to the following general explanation of the structure in these profiles. The asymmetry between the critical and the noncritical planes is due to walk-off of the resonated signal beam. This walk-off leads to a small acceptance angle (0.88 mrad) in the critical plane that restricts the range of off-axis k vectors that have gain. At the lower pump fluence the signal beam is single peaked (like the pump) and is elliptical in shape because of different divergences in the critical and the noncritical planes. At the higher fluence the signal and the idler generated in the center of the pump beam can completely deplete the pump beam and can backconvert to generate new pump. Thus the signal beam is somewhat depleted on axis because of backconversion. The amount of backconversion varies with position in the beam, and this spatial modulation creates off-axis k vectors. The small acceptance

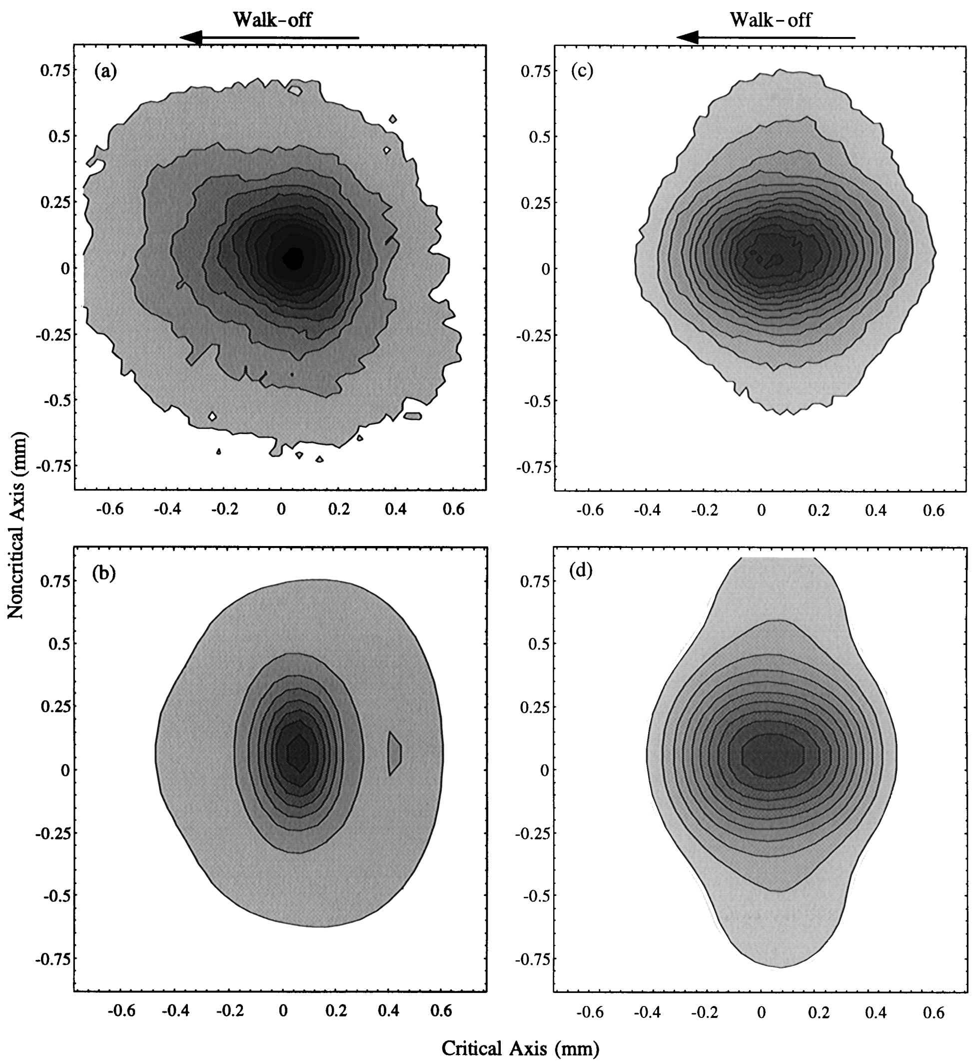

Fig. 5. Measured [(a), (c)] and calculated [(b), (d)] contour plots of the fluence spatial profiles of the depleted pump [(a), (b)] and the signal [(c), (d)] beams measured 30 cm from the OPO output mirror when the OPO is pumped at 1.6 $\mathrm{J/cm^2}$ (2.3 times threshold), and the phase mismatch is zero. The peak measured (calculated) depleted pump fluence is 1.17 (0.84) $\mathrm{J/cm^2}$, and each contour is separated by 0.1 $\mathrm{J/cm^2}$. The peak measured (calculated) signal fluence is 0.67 (0.53) $\mathrm{J/cm^2}$, and each contour is separated by 0.05 $\mathrm{J/cm^2}$.

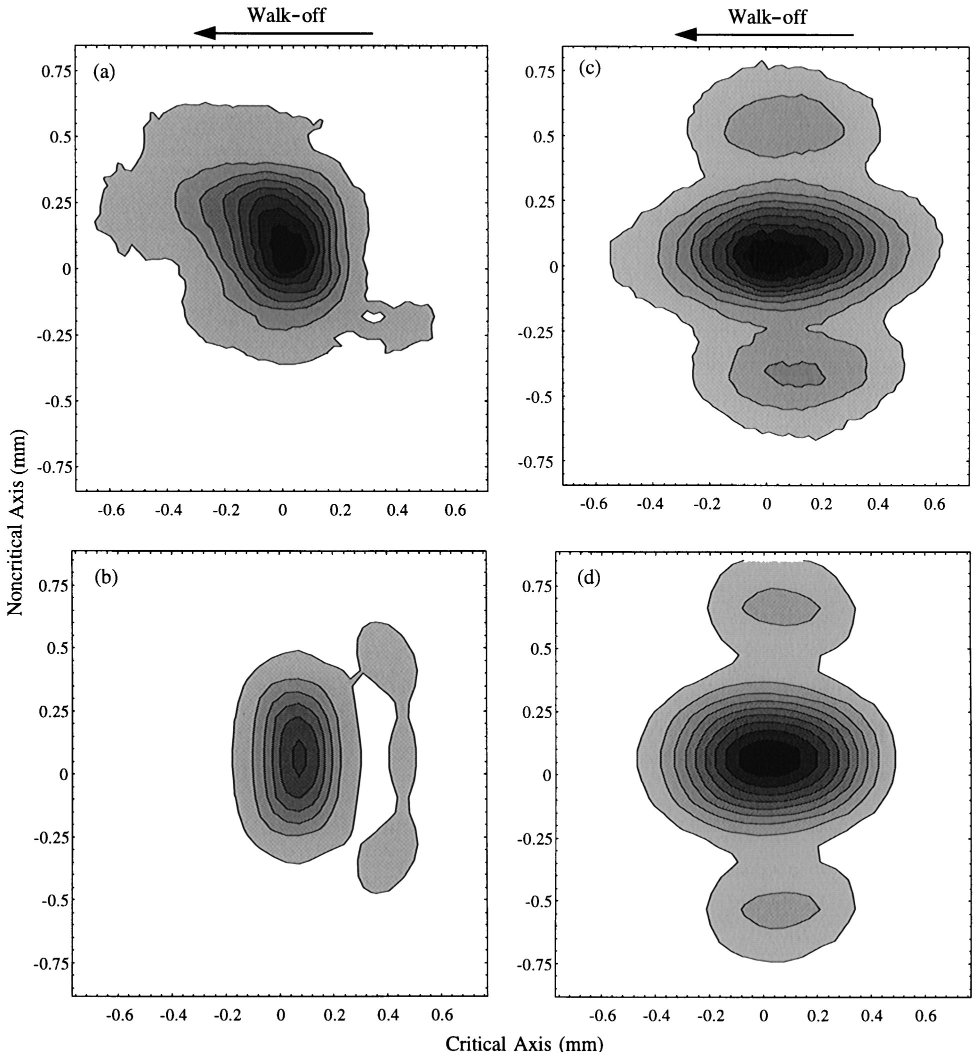

Fig. 6. Measured [(a), (c)] and calculated [(b), (d)] contour plots of the fluence spatial profiles of the depleted pump [(a), (b)] and the signal [(c), (d)] beams measured 30 cm from the OPO output mirror, when the OPO is pumped at 2.5 J/cm^2 (3.5 times threshold), and the phase mismatch is zero. The peak measured (calculated) depleted pump fluence is 2.27 (1.55) J/cm^2 and the contours are separated by 0.25 J/cm^2. The peak measured (calculated) signal fluence is 0.95 (0.97) J/cm^2, and each contour is separated by 0.1 J/cm^2.

angle in the critical plane means that the off-axis k vectors in that direction see much lower gain than do those in the noncritical direction. Hence the lobes grow more readily in the noncritical plane.

D. Beam Quality

The signal beam contours qualitatively indicate that the beam quality degrades as the pump fluence increases and that the beam quality is better in the critical plane than in the noncritical plane. We quantified these effects by measuring the beam-quality factor M^2 in both the critical and the noncritical planes. These results are shown in Fig. 7 along with calculated values of M^2 (curves). The beam quality in the critical plane is much better than in the noncritical plane at the higher fluence of 2.5 J/cm^2. This asymmetry in beam quality can be important for applications requiring subsequent nonlinear conversion of the OPO output.

E. Power

Figures 8 and 9 display measured and computed full-beam power profiles at pumping levels of 1.6 and 2.5 J/cm^2. As expected, the turn-on time at the higher pump fluence is earlier than at the lower pump fluence. The signal and the idler profiles are smooth single peaks

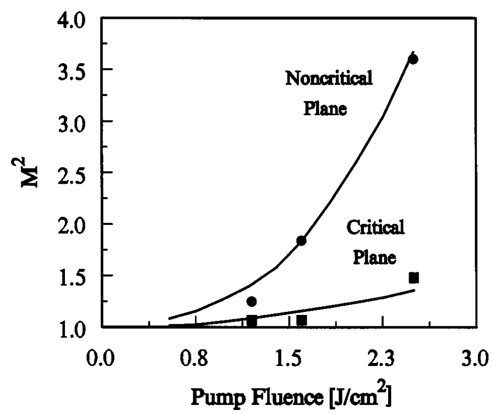

Fig. 7. Beam-quality factor M^2 for various pump fluences. The symbols represent the experimental data, and the curves are model predictions. The better beam quality in the critical direction is caused by the strong angular dependence of the gain in the critically phase-matched KTP crystal.

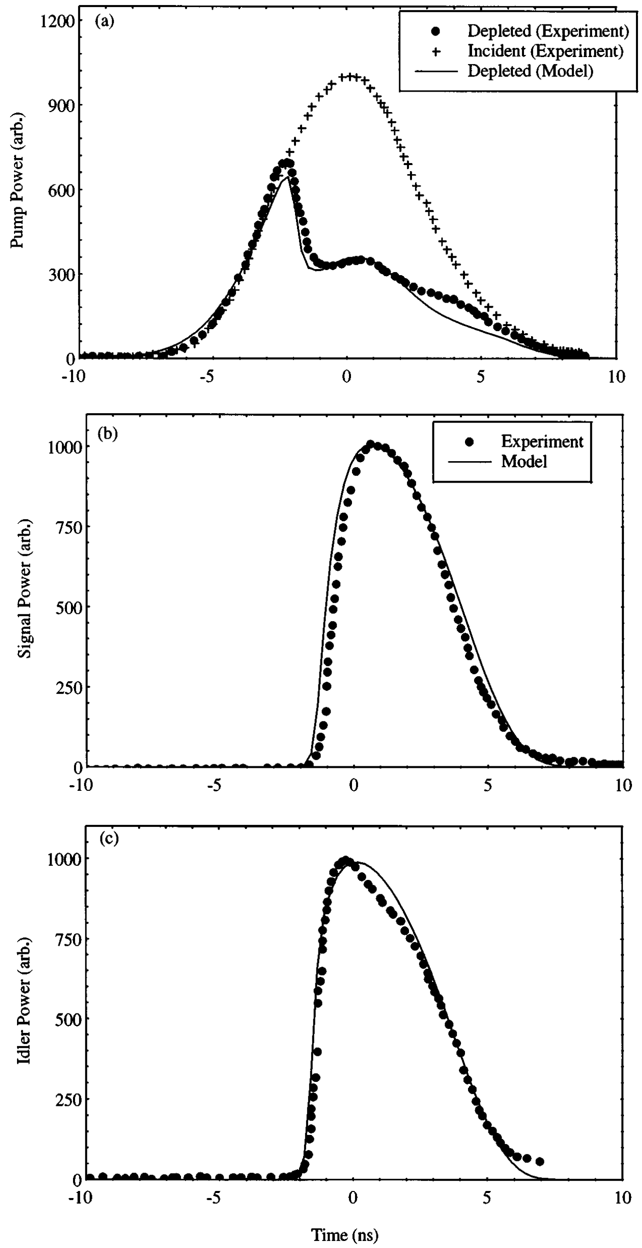

Fig. 8. Spatially integrated power profiles of (a) the incident and the depleted pump, (b) the signal beam, and (c) the idler beam when the OPO is pumped at 1.6 J/cm^2 (2.3 times threshold).

for both pump fluences. The depleted pump profiles, however, show a secondary peak centered near 0 ns that indicates backconversion. This peak is larger at the higher pump level, as expected.

Agreement between experiment and model is good at this level. A more stringent test of the model's accuracy and stronger evidence of backconversion are provided by spatially resolved power profiles. These profiles are shown in Figs. 10, 11, and 12 for pump fluence of 1.6 J/cm^2 at various locations within the pump, the signal, and the idler beams, respectively. We obtained them by imaging the OPO output onto a small aperture and recording the transmitted power, using fast detectors. The depleted pump profiles (Fig. 10) show clear evidence of backconversion. The time profile of the center of the pump beam shows a strong backconversion peak centered at 1 ns. Profiles in the wings of the pump beam show much less backconversion because of the smaller pump intensities and the resulting lower gain. Thus the pump is converting to signal and idler more efficiently in the wings than in the center of the pump beam. Data obtained at a pump level of 2.5 J/cm^2 (not shown) show an even greater backconversion peak at the center of the pump beam. The spatially resolved power profiles of the signal and the idler are rather unstructured compared with the depleted pump profiles but also agree reasonably well with the model. It is worth noting, however, that the idler profiles are different from the signal because

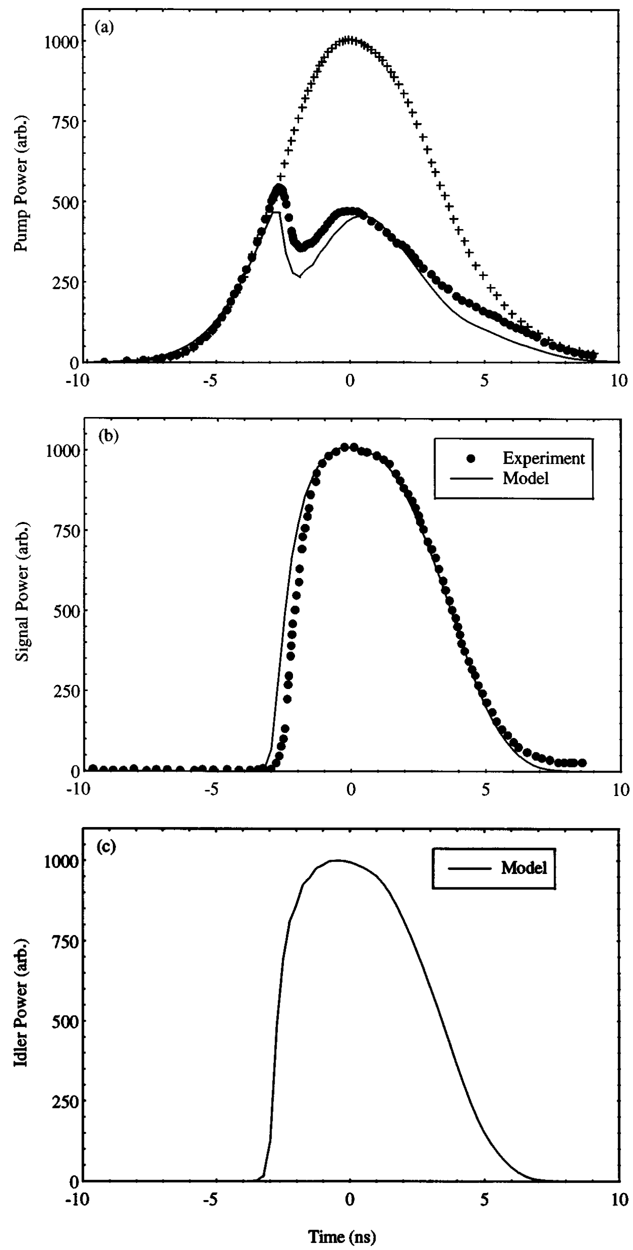

Fig. 9. Spatially integrated power profiles of (a) the incident and the depleted pump, (b) the signal beam, and (c) the idler beam when the OPO is pumped at 2.5 J/cm^2 (3.6 times threshold). Note: an experimental profile for the idler is not available.

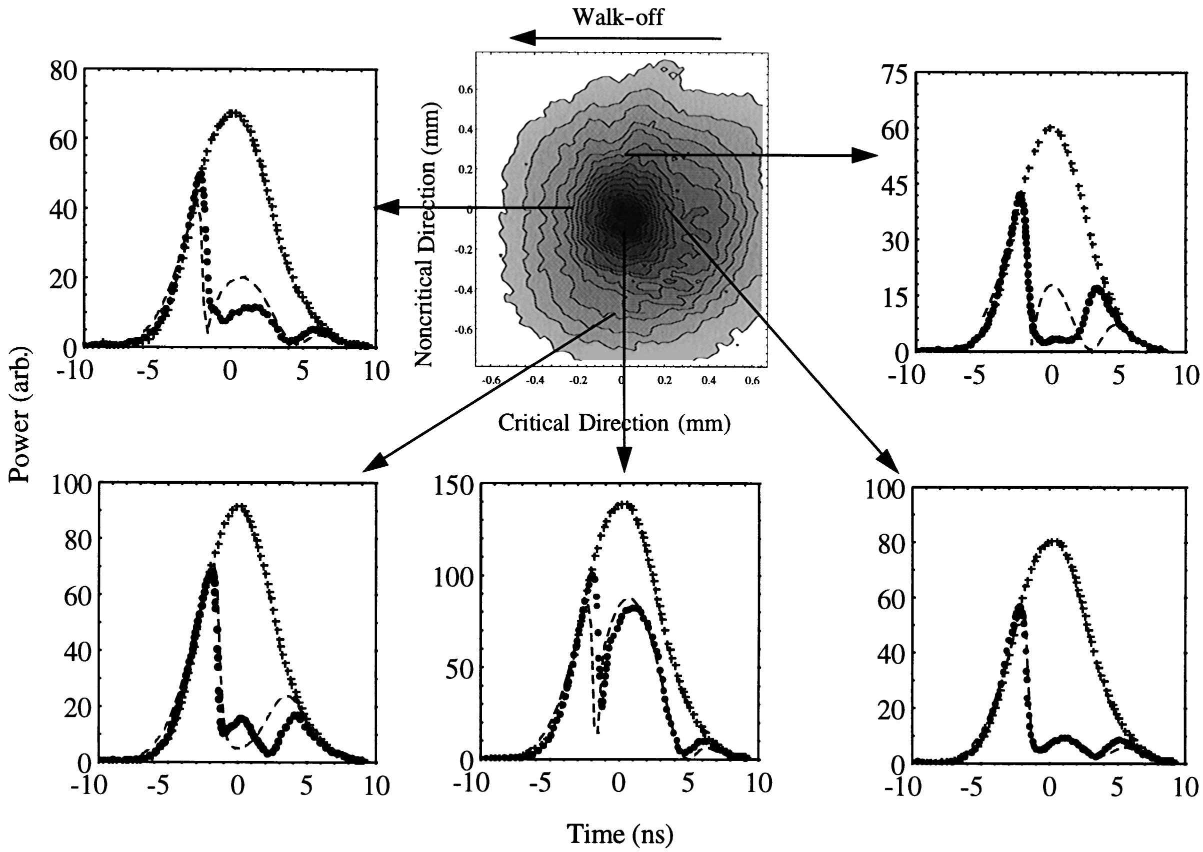

Fig. 10. Measured fluence profile of the depleted pump and spatially resolved power profiles at locations in the beam indicated by the arrows. Shown are wave forms for the incident pump (+'s) the depleted pump (dots), and the calculated depleted pump (dashed curves). The incident pump fluence is 1.6 J/cm^2 (2.3 times threshold).

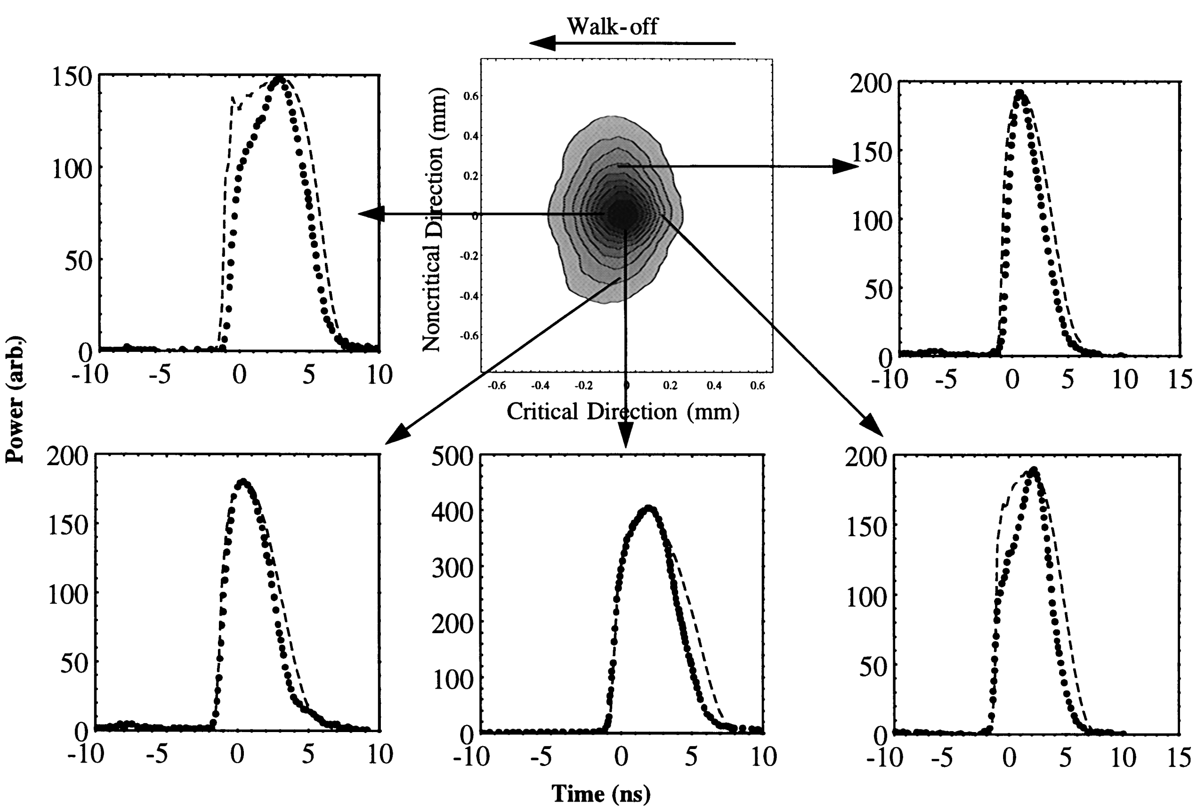

Fig. 11. Measured fluence profile of the signal and spatially resolved power profiles at locations in the beam indicated by the arrows. Shown are wave forms for the measured (dots) and the calculated (dashed curves) signal-wave forms. The incident pump fluence is 1.6 J/cm^2 (2.3 times threshold). The signal peak fluence is 0.54 J/cm^2.

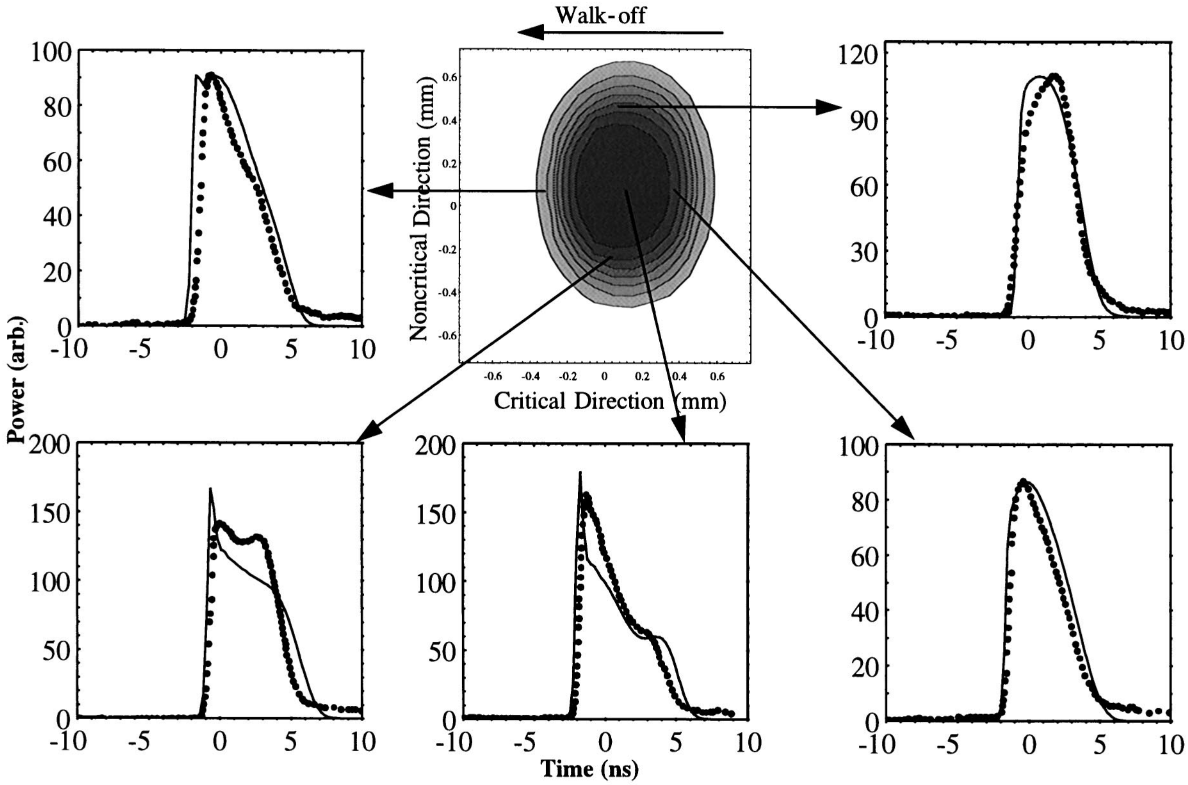

Fig. 12. Calculated energy fluence profile of the idler and spatially resolved power profiles at locations in the beam indicated by the arrows. An experimental spatial profile was not available. Shown are the wave forms for the measured (dots) and the calculated (curves) idler-wave forms. The incident pump fluence is 1.6 J/cm^2 (2.3 times threshold). The idler peak fluence is calculated to be 0.2 J/cm^2.

the signal is resonated in the OPO cavity and thus gets averaged over a few round-trip times.

F. Spectra

Spectra of the entire (spatially integrated) signal beam are shown in Fig. 13 for pump levels of 1.6 and 2.5 J/cm^2. The signal spectrum at the lower pump level is quite close to the Fourier transform of the spatially integrated time profile of the signal, i.e., the signal is very nearly transform limited. At the higher pump level, however, the spectrum deviates significantly from the transform limit. The laboratory spectrum is shifted and is broadened. These changes result from time-dependent phase shifts, created by backconversion, that vary across the spatial profile of the signal beam. Because the whole-beam spectrum is the sum of spectra for all the spatial locations of the beam and because each of these locations can have different amplitude and phase time profiles, deviations from the transform of the whole-beam time profile are not surprising.

Figure 14 shows spectra for the entire pump beam corresponding to the signal spectra shown in Fig. 13. In contrast to the signal spectra, both pump spectra show significant deviation from the transform of the whole-beam time profile. One would expect the pump spectra to show stronger backconversion effects because the pump beam's time profiles vary significantly with transverse position in the beam, as we showed in Fig. 10. In addition, because the backconversion peak is produced with a π phase shift relative to the incident pump, one expects a doubletlike spectrum in the heavily backconverted parts of the beam. The shoulders on the sides of the spectra shown in Fig. 14 are clear evidence of this doublet.

G. Nonzero Phase Mismatch

All the data presented above were taken with zero phase mismatch. It is instructive to look at the OPO performance when the phase mismatch is nonzero. Figure 15 shows spatial contours of the pump [Figs. 15(a) and 15(b)]

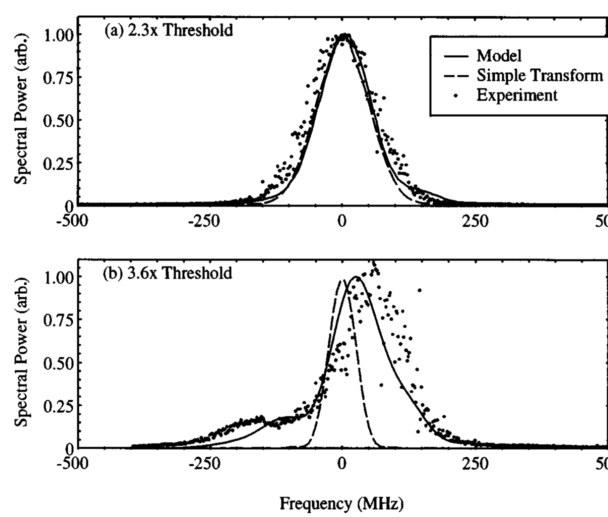

Fig. 13. Spectra of the signal for pump levels (in J/cm^2) of (a) 1.6 and (b) 2.5. The dots represent the measured spectra, and the solid curves are the model predictions. The dashed curves show the Fourier transform of the spatially integrated time profiles.

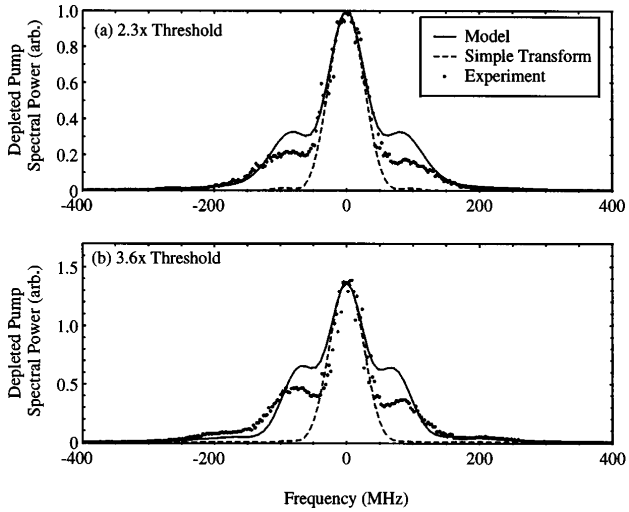

Fig. 14. Spectra of the depleted pump at pump levels (in J/cm^2) of (a) 1.6 and (b) 2.5. The dots represent the measured spectra, and the solid curves are the model predictions. The dashed curves show the Fourier transform of the spatially integrated time profiles.

and the signal [Figs. 15(c) and 15(d)] at a pump level of 2.5 J/cm^2, with $\Delta kL = -0.64$. Figure 16 is the same, but with $\Delta kL = +2.88$. We find that the depleted pump beam is defocusing (focusing) for negative (positive) phase mismatch. This effect is quite noticeable in Fig. 16(a), in which the measured depleted pump beam has a higher peak fluence (3.2 J/cm^2) than the incident pump beam (2.5 J/cm^2). Focusing and defocusing are the result of curvature impressed on the wave front by intensity-dependent phase shifts associated with nonzero Δk.[31]

The spectrum of an injection-seeded OPO with phase mismatch is an interesting topic that was briefly discussed previously.[11,33] The existence of phase mismatch causes a phase shift of the resonated wave of order ΔkL on each pass through the nonlinear crystal. Because the phase shift occurs on each round trip, the amplified resonated wave is frequency shifted relative to the seed wave. Figure 17 shows the signal spectrum for negative, zero, and positive values of Δk at a pump level of 1.6 J/cm^2. The measured sign of the frequency shift is opposite that of Δk. These shifts are approximately linear in Δk and increase with increasing pump fluence.[33] We also find that the shifted peaks are broadened rela-

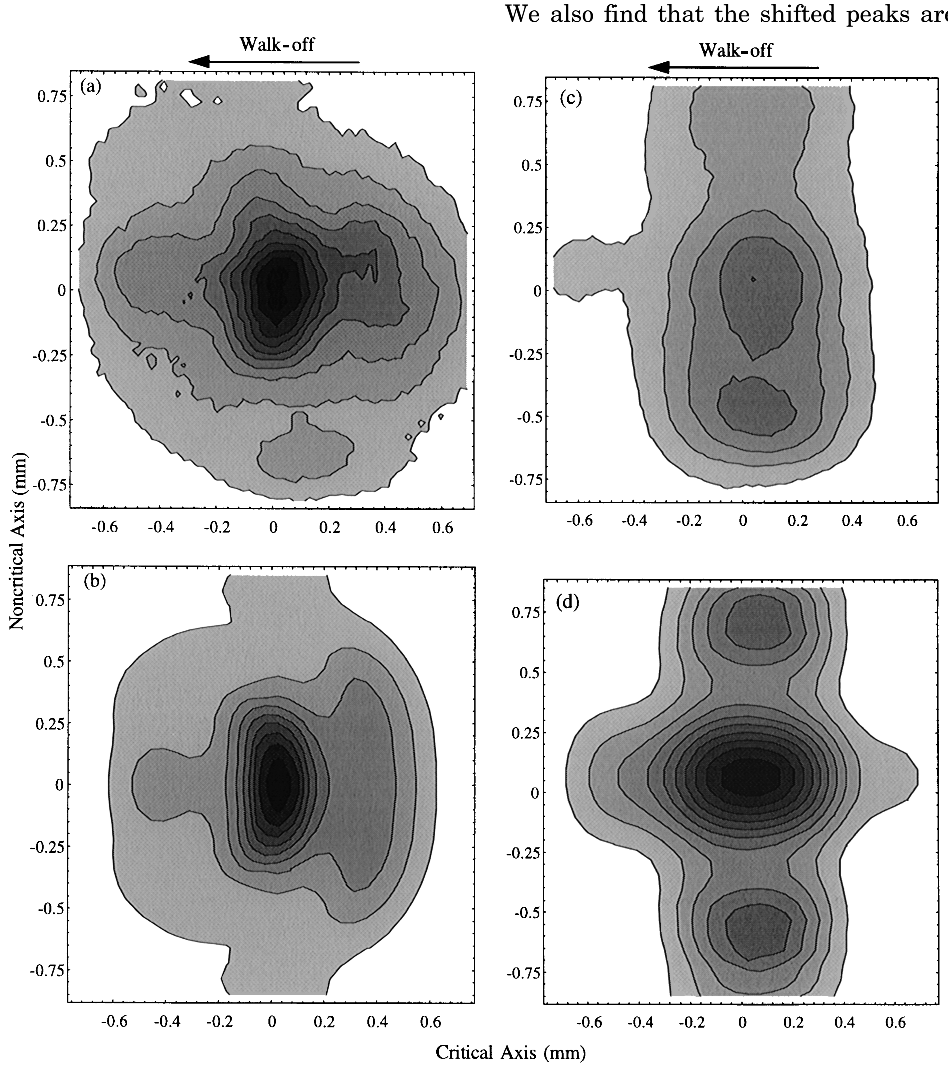

Fig. 15. Measured [(a), (c)] and calculated [(b), (d)] contour plots of the energy fluence profiles of the depleted pump [(a), (b)] and the signal [(c), (d)] beams when a phase mismatch is intentionally introduced by rotation of the KTP crystal. The OPO is pumped at 2.5 J/cm^2, and the phase mismatch, ΔkL, is -0.64. The peak measured (calculated) depleted pump fluence is 1 (1.0) J/cm^2, and the contours are separated by 0.1 J/cm^2. The peak measured (calculated) signal fluence is 0.25 (0.53) J/cm^2, and the contours are separated by 0.05 J/cm^2.

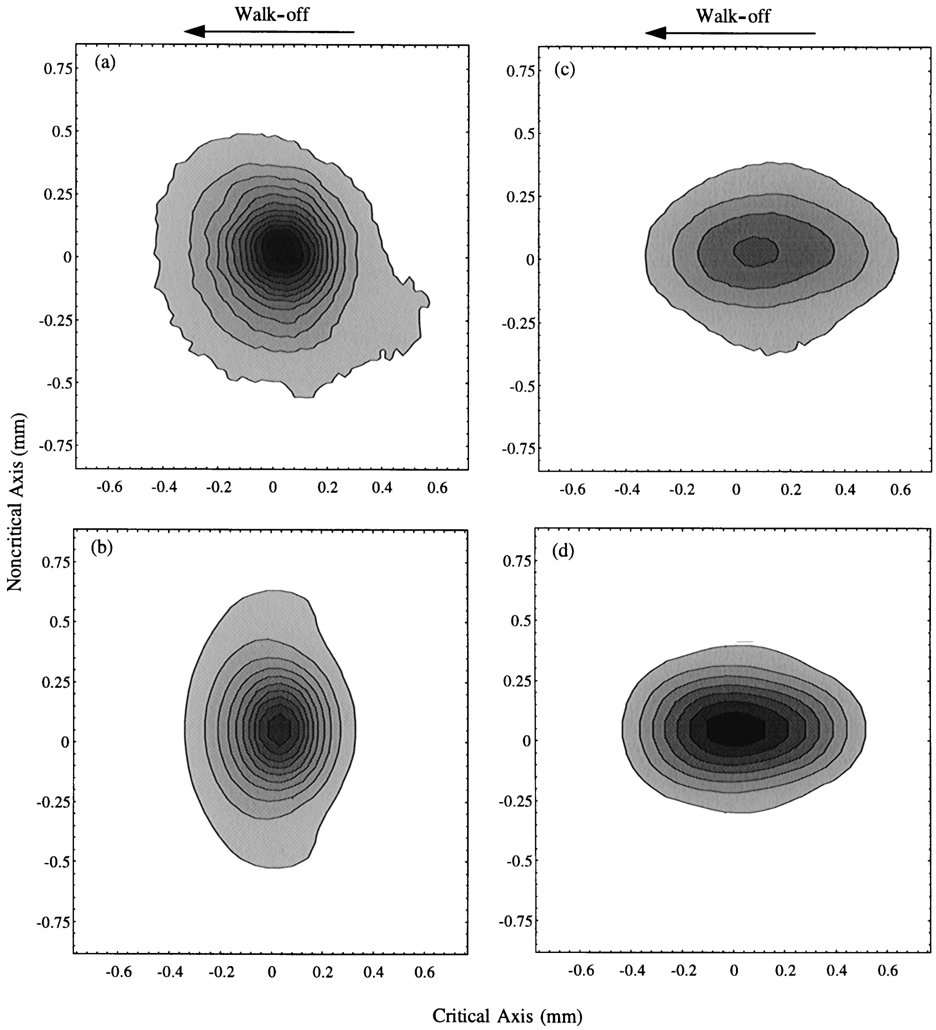

Fig. 16. Measured [(a), (c)] and calculated [(b), (d)] contour plots of the energy fluence profiles of the depleted pump [(a), (b)] and the signal [(c), (d)] beams when a phase mismatch is intentionally introduced by rotation of the KTP crystal. The OPO is pumped at 2.5 J/cm^2, and the phase mismatch, ΔkL, is +2.88. The peak measured (calculated) depleted pump fluence is 3.1 (2.65) J/cm^2, and the contours are separated by 0.25 J/cm^2. The peak measured (calculated) signal fluence is 0.42 (0.76) J/cm^2, and the contours are separated by 0.1 J/cm^2.

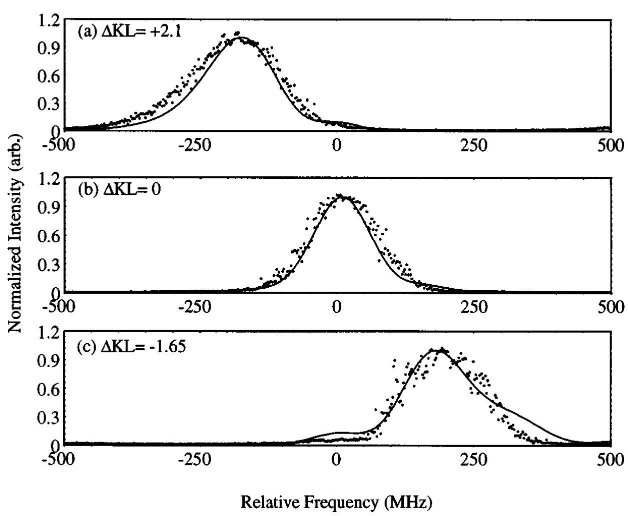

Fig. 17. Spectra of the signal beam for different values of phase mismatch. The measured (dots) and the calculated (curves) profiles are shown for ΔkL values of (a) +2.1, (b) 0.0, and (c) −1.65. The OPO is pumped at 1.6 J/cm^2.

tive to the unshifted, $\Delta k = 0$, peak. Note that even modest values of ΔkL, which diminish the output energy by only 10%, are sufficient to cause frequency shifts comparable with the linewidth of the pulsed light. Such shifts could be important in high-resolution spectroscopic applications. At higher pump fluences the peaks are not only broadened but can develop significant structure, as illustrated in Fig. 18, which shows the signal spectrum at a pump level 3.6 times threshold with small negative phase mismatch.

The agreement between model calculations and experiments with nonzero phase mismatch is generally worse at the higher fluence, as can be seen by comparison of Figs. 17 and 18. We also observed, in both the laboratory and the model, features in the power profiles of the depleted pump at the center of the pump beam that occur on the time scale of a cavity round-trip time. Because the model uses the round-trip time as the time increment, we may not be resolving all the time features and thus may not be accurately predicting spectra. The laboratory spectra are recorded by use of flat mirror étalons and are probably more accurate than the model.

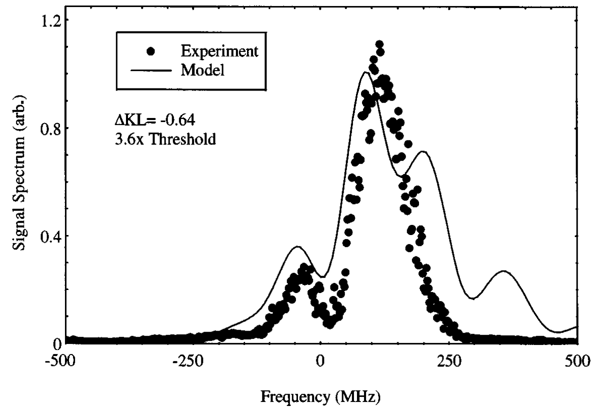

Fig. 18. Spectrum of the signal beam with $\Delta kL = -0.64$ and the OPO pumped at 2.5 J/cm^2.

5. CONCLUSIONS

We have developed a model of nanosecond, injection-seeded OPO's that includes all the relevant physics of these devices, including walk-off, diffraction, and pump depletion. We have also built a laboratory ring-cavity, KTP OPO and have carefully characterized all the physical parameters relevant to its performance. We presented here a comparison of laboratory measurements and model predictions of OPO efficiency, thresholds, spatially resolved and full-beam power profiles, signal and pump spectra, fluence profiles, and signal beam quality. In our comparison, we used only measured values for the input parameters to the model. We did not vary them to improve agreement between model and experiment, yet we find good qualitative agreement of model and experiment in all the cases, and we usually have good quantitative agreement as well.

Our major conclusion concerning the operation of nanosecond OPO's is that backconversion (conversion of signal and idler back to pump) affects all aspects of performance. It limits OPO efficiency and degrades the spectrum and the beam quality. Furthermore, backconversion is almost always present in nanosecond OPO's because the single-pass gain must be very high to reach threshold during a single pulse. Once threshold is reached, however, the high gain usually completely depletes the center of the pump beam and allows the signal and the idler to backconvert. The effects of backconversion are minimized at pump levels just above threshold.

We conclude that, based on our results, conversion efficiency can be rather high (quantum efficiency of approximately 50%) but levels off at high pump fluences because of backconversion. Furthermore, the quality of the output beam degrades at higher pump fluences and is generally better in the critical plane than in the noncritical plane because of the crystal's small acceptance angle in the critical plane. In addition, the output spectra can be broadened and shifted at high pump fluences, and phase-mismatch-induced shifts can be greater than the linewidth of the OPO output.

We are convinced by the agreement between model and experiment that the model should prove a useful tool in designing and developing improved OPO's. We intend to use it to explore methods of improving OPO beam quality, such as new resonator designs, pump geometries, etc.

Finally, we note that the primary limitations of the model are that it does not allow for frequency-selective intracavity elements and that it does not handle unseeded operation accurately. At present, it does not resolve time structure shorter than the round-trip time of the cavity, but one can rectify that difficulty by interleaving time slices.

APPENDIX A: TYPICAL OPTICAL PARAMETRIC OSCILLATOR PARAMETERS IN MODEL AND MEASUREMENTS

Table 1 lists typical operating parameters used in modeling the OPO. All these parameters were measured or were estimated for the laboratory device. Here we describe each parameter and discuss the measurement methods and uncertainties.

L_{crystal} is the physical length of the KTP crystal. d_{eff} is the effective nonlinear coefficient appropriate for the propagation angle and polarizations used in our device. This value was found by measurement of single-pass gain in the actual crystal used in the OPO. We estimate the uncertainty of the measurement at 5%. Δk is the wave-vector mismatch in the crystal. It was calculated as a function of angle with Sellmeier equations[34] that accurately describe the angular tuning of KTP OPO's. We located the zero point of Δk by finding the angle of minimum threshold. n_2 is the nonlinear coefficient of the refractive index, for which a value of 2.4×10^{-15} was given by DeSalvo *et al.*[35] We find that including this value has no effect on OPO model results, so it is normally set to

Table 1. Typical OPO Parameters

Parameter	Value	Parameter	Value
L_{crystal} (mm)	10.0	d_{eff} (pm/V)	2.9
Δk (cm^{-1})	−2.14 to +2.88	n_2 (cm^2/W)	0.0
U_{pump} (mJ)	7.4, 11.6	λ_{pump} (nm)	532
λ_{signal} (nm)	780	λ_{idler} (nm)	1673.23
R^i_{pump} (mm)	0.51	R^o_{pump} (mm)	0.58
n_{signal}	1.81625	n_{idler}	1.73462
n_{pump}	1.79030	θ_{signal} (mrad)	51.0
θ_{idler} (mrad)	0.0	θ_{pump} (mrad)	0.0
δ^i_{pump} (mm)	0.0	$\delta^i_{\text{signal seed}}$ (mm)	0.0
$\delta^o_{\text{signal seed}}$ (mm)	0.0	R_{signal} (mm)	0.73
$P_{\text{signal seed}}$ (W)	0.025	N_x	32
N_y	32	X_{maximum} (mm)	1.4
Y_{maximum} (mm)	1.5	L_{ring} (mm)	67
$L_{\text{crystal leg}}$ (mm)	25	O/E	odd
$R1_{\text{signal}}$	0.99	$R1_{\text{idler}}$	0.01
$R1_{\text{pump}}$	0.04	$R2_{\text{signal}}$	0.51
$R2_{\text{idler}}$	0.01	$R2_{\text{pump}}$	0.18
$R3_{\text{signal}}$	0.99	$R3_{\text{idler}}$	0.01
$R3_{\text{pump}}$	0.04	α_{signal} (mm^{-1})	0.0
α_{idler} (mm^{-1})	0.0	α_{pump} (mm^{-1})	0.00513
$\text{RC}_{\text{signal}}$	0.01	RC_{idler}	0.01
RC_{pump}	0.02	$\phi 1_{\text{signal}}$ (rad)	0.0
$\phi 1_{\text{idler}}$ (rad)	0.0	$\phi 1_{\text{pump}}$ (rad)	0.0
$\phi 2_{\text{signal}}$ (rad)	0.0	$\phi 2_{\text{idler}}$ (rad)	0.0
$\phi 2_{\text{pump}}$ (rad)	0.0	T_{start} (round trips)	−40
T_{stop} (round trips)	40	$\text{Tilt}_{\text{pump}}$ (mrad)	0.0
β_{pump} (mm/GW)	0.0	τ_{pump} (ns)	7.0

zero. The pump energy U_{pump} is accurate to 5%. The pump beam is slightly elliptical, so we specify two orthogonal beam radii. The radius, R^i_{pump}, is the $1/e^2$ intensity radius in the plane of the ring, and R^o_{pump} is the radius out of the plane. The uncertainty of the Gaussian fits to the actual beam profile is approximately 10%. The refractive indices, n, and the walk-off angles, θ, are all derived from the Sellmeier equations cited above. The δ^i values are displacements from the ring-cavity axis in the plane of the ring. $\delta^o_{\text{signal seed}}$ is the displacement of the seed beam from the pump beam perpendicular to the plane of the ring. The uncertainty is approximately 0.1 mm. R_{signal} is the radius ($1/e^2$) of the seed beam, accurate to 10%. The seed power $P_{\text{signal seed}}$ is accurate to 10%. The number of grid points N_x and N_y is typically 64. We vary these from 32 to 128 to check convergence of the model results. X_{maximum} and Y_{maximum} are half the full spatial extent of the model grid. L_{ring} is the full physical length of the cavity. $L_{\text{crystal leg}}$ is the length of the leg of the ring containing the crystal. This parameter is used only to calculate the curvature of the pump beam at the input mirror necessary to produce the specified pump spot size at the center of the crystal. For the beam sizes used here, this parameter is not important. The parameter O/E specifies whether the optical cavity has an odd or an even number of mirrors. For an odd number, the beams invert in the plane of the ring on each round trip, whereas for an even number of mirrors they do not. Here we use only an odd number of mirrors. The R's are the reflectivities of the three cavity mirrors. The pump values for $R1$ (the pump input mirror) and $R2$ (the signal output mirror) were measured, as was the signal value for $R2$. The remainder are estimates. The α's are linear absorption coefficients in the crystal. The pump value is deduced from a measurement of the crystal transmission. The others are known to be small. The crystal face reflectivities are denoted by RC. The crystal is antireflection coated for the signal and the pump, but not for the idler. The signal reflectivity is 1% or less, but the pump reflectivity is approximately 2%. The idler reflectivity is unknown. The phase shifts, ϕ, are in two parts: the first, $\phi 1$, is the shift over the path from the input mirror to the crystal; the second is from the crystal output face to the input mirror. Only the signal phase is important here because it is the only wave resonated. This parameter is nonzero only when the cavity is not resonant with the seed light. It is always zero for this study. The start time and the stop time are specified by T_{start} and T_{stop}, respectively, measured in cavity round-trip time. The tilt of the pump relative to the cavity axis, $\text{Tilt}_{\text{pump}}$, is always zero. The two-photon absorption coefficient, β, is 0.1 cm/GW (Ref. 35), and we set it to zero. The duration of the pump pulse (FWHM intensity), τ_{pump}, is approximately 7.0 ns. This value can vary from day to day. It is routinely measured to 8%, and the actual value is used in comparisons.

ACKNOWLEDGMENTS

We thank Ron Allman for his fine technical support of the experiments. This research is supported by the U.S. Department of Energy under contract DE-AC04-94AL85000.

REFERENCES

1. J. A. Giordmaine and R. C. Miller, "Tunable coherent parametric oscillation in $LiNbO_3$ at optical frequencies," Phys. Rev. Lett. **14,** 973–976 (1965).
2. Y. Cui, D. E. Withers, C. G. Rae, C. J. Norrie, Y. Tang, B. D. Sinclair, W. Sibbett, and M. H. Dunn, "Widely tunable all-solid-state optical parametric oscillator for the visible and near infrared," Opt. Lett. **18,** 122–124 (1993).
3. K. Kato, "Parametric oscillation in LiB_3O_5 pumped at 0.532 μm," IEEE J. Quantum Electron. **26,** 2043–2045 (1990).
4. Y. Tang, Y. Cui, and M. H. Dunn, "Lithium triborate optical parametric oscillator pumped at 266 nm," Opt. Lett. **17,** 192–194 (1992).
5. G. Robertson, A. Henderson, and M. H. Dunn, "Attainment of high efficiencies in optical parametric oscillators," Opt. Lett. **16,** 1584–1586 (1991).
6. F. Hanson and D. Dick, "Blue parametric generation from temperature-tuned LiB_3O_5," Opt. Lett. **16,** 205–207 (1991).
7. G. J. Hall and A. I. Ferguson, "LiB_3O_5 optical parametric oscillator pumped by a Q-switched frequency-doubled all-solid-state laser," Opt. Lett. **18,** 1511–1513 (1993).
8. N. P. Barnes, K. E. Murray, and G. H. Watson, "Injection-seeded optical parametric oscillator," in *Advanced Solid-State Lasers*, Vol. 13 of 1992 OSA Proceedings Series, L. L. Chase and A. A. Pinto, eds. (Optical Society of America, Washington, D.C., 1992), pp. 356–360.
9. P. A. Budni, M. G. Knights, E. P. Chicklis, and K. L. Shepler, "Kilohertz $AgGaSe_2$ optical parametric oscillator pumped at 2 μm," Opt. Lett. **18,** 1068–1070 (1993).
10. M. J. T. Milton, T. D. Gardiner, G. Chourdakis, and P. T. Woods, "Injection seeding of an infrared optical parametric oscillator with a tunable diode laser," Opt. Lett. **19,** 281–283 (1994).
11. D. C. Hovde, J. H. Timmermans, G. Scoles, and K. K. Lehman, "High power injection seeded optical parametric oscillator," Opt. Commun. **86,** 294–300 (1991).
12. W. R. Bosenberg and R. H. Jarman, "Type-II phase-matched $KNbO_3$ optical parametric oscillator," Opt. Lett. **16,** 1323–1325 (1993).
13. M. Ebrahimzadeh, A. J. Henderson, and M. H. Dunn, "An excimer-pumped β-BaB_2O_3 optical parametric oscillator tunable from 354 nm to 2.370 μm," IEEE J. Quantum Electron. **26,** 1241–1252 (1990).
14. W. R. Bosenberg, W. S. Pelouch, and C. L. Tang, "High-efficiency and narrow-linewidth operation of a two-crystal β-BaB_2O_3 optical parametric oscillator," Appl. Phys. Lett. **55,** 1952–1954 (1989).
15. W. R. Bosenberg, L. K. Cheng, and C. L. Tang, "Ultraviolet optical parametric oscillation in β-BaB_2O_3," Appl. Phys. Lett. **54,** 13–15 (1989).
16. M. D. Turner, L. Hanko, and M. J. McAuliffe, "Synchronously pumped gigahertz modulated optical parametric oscillator," J. Opt. Soc. Am. B **11,**632–635 (1994).
17. K. Kato and M. Masutani, "Widely tunable 90° phase-matched KTP parametric oscillator," Opt. Lett. **17,** 178–180 (1992).
18. J. T. Lin and J. L. Montgomery, "Generation of tunable mid-IR (1.8–2.4 μm) laser from optical parametric oscillation in KTP," Opt. Commun. **75,** 315–320 (1990).
19. W. R. Bosenberg and D. R. Guyer, "Single-frequency optical parametric oscillator," Appl. Phys. Lett. **61,** 387–389 (1992).
20. L. R. Marshall, A. Kaz, and O. Aytur, "Continuously tunable diode-pumped UV–blue laser source," Opt. Lett. **18,** 817–819 (1993).
21. S. J. Brosnan and R. L. Byer, "Optical parametric oscillator threshold and linewidth studies," IEEE J. Quantum Electron. **QE-18,** 415–431 (1979).
22. S. Guha, F.-J. Wu, and J. Falk, "The effects of focusing on parametric oscillation," IEEE J. Quantum Electron. **QE-18,** 907–912 (1982).
23. J. A. C. Terry, Y. Cui, Y. Yang, W. Sibbett, and M. H. Dunn, "Low-threshold operation of an all-solid-state KTP optical parametric oscillator," J. Opt. Soc. Am. B **11,**758–769 (1994).
24. J. M. Breteau, C. Jourdain, T. Lepine, and F. Simon, "Nu-

merical simulation and realization of a KTP optical parametric oscillator," in *Advanced Solid-State Lasers*, Vol. 20 of 1993 OSA Proceedings, A. A. Pinto and T. Y. Fan, eds. (Optical Society of America, Washington, D.C., 1993), pp. 118–120.

25. A. E. Siegman, "Defining the effective radius of curvature for a nonideal optical beam," IEEE J. Quantum Electron. **27,** 1146–1148 (1993).
26. A. E. Siegman, "New developments in laser resonators," in *Optical Resonators*, D. A. Holmes, ed., Proc. Soc. Photo-Opt. Instrum. Eng. **1224,** 2–14 (1990).
27. M. A. Dreger and J. K. McIver, "Second-harmonic generation in a nonlinear, anisotropic medium with diffraction and depletion," J. Opt. Soc. Am. B **7,** 776–784 (1990).
28. M. Nieto-Vesperinas and G. Lera, "Solution to nonlinear optical mixing equations with depletion and diffraction: difference-frequency generation," Opt. Commun. **69,** 329–333 (1980).
29. S. S. Ma, D. M. Guthals, B. F. Campbell, and P. H. Hu, "Three-dimensional anisotropic physical optics modeling of three wave mixing," in *Laser Resonators and Coherent Optics: Modeling, Technology, and Applications*, A. Bhowmik, ed., Proc. Soc. Photo-Opt. Instrum. Eng. **1868,** 135–141 (1993).
30. P. Pliszka and P. P. Banerjee, "Nonlinear transverse effects in second-harmonic generation," J. Opt. Soc. Am. B **10,** 1810–1819 (1993).
31. A. V. Smith and M. S. Bowers, "Phase distortions in sum- and difference-frequency mixing in crystals," J. Opt. Soc. Am. B **12,** 49–57 (1995).
32. W. H. Press, S. A. Teukolsky, W. T. Vettering, and B. P. Flannery, *Numerical Recipes in FORTRAN* (Cambridge U. Press, New York, 1992), pp. 704–716.
33. T. D. Raymond, W. J. Alford, A. V. Smith, and M. S. Bowers, "Frequency shifts in injection-seeded optical parametric oscillators with phase mismatch," J. Opt. Soc. Am. B **19,** 1520–1522 (1994).
34. J. D. Bierlein and H. Vanherzeele, "Potassium titanyl phosphate: properties and new applications," J. Opt. Soc. Am. B **6,** 622–633 (1989).
35. R. DeSalvo, D. J. Hagan, M. Sheik-Bahae, G. Stegeman, and E. W. Van Stryland, "Self-focusing and self-defocusing by cascaded second-order effects in KTP," Opt. Lett. **17,** 28–30 (1992).